Cardiac Bidomain Bath-Loading Effects During Arrhythmias: Interaction with Anatomical Heterogeneity
Supporting Material

Martin J. Bishop, Edward J. Vigmond, Gernot Plank

August 2011

1 Methods

1.1 Computational Models

1.1.1 Geometrically Simplified Cardiac Slab Model

A cuboid, tetrahedral finite element model, of dimensions 3.0 cm × 3.0 cm × 0.5 cm and a spatial discretisation step $h = 200$ μm, was used to represent a 3D slab of myocardial tissue [1, 2]. An additional representation of a perfusing bath, of thickness 0.1 cm in the z-direction, was included representing conducting medium in contact with the epi-/endocardial surfaces, as shown in Figure 1(a). Anisotropic conduction was assigned through a locally-prevailing cardiac fibre architecture which either varied transmurally between ±60 degrees (relative to x-axis) from epi- to endocardium or a constant fibre orientation of 0 degrees was assigned throughout the myocardium, i.e. fibres parallel to the x-axis (shown in Figure 1(a)).

1.1.2 Anatomically-Complex Rabbit Ventricular Model

In addition, a previously published high-resolution finite element model of the rabbit ventricles [3] was also used, containing a high degree of anatomical complexity, including representations of blood vessel cavities and extracellular cleft spaces, as well as endocardial structures (papillary muscles and trabeculations) shown in Figure 1(b). The myocardial ventricular mesh measures approximately 29 mm in the apex-base direction, and sits within a perfusing bath, filling the ventricular and all intramural cavities. Although variable, much of the LV free wall is approximately $4-6$ mm thick, compared to $1-2$ mm in the RV.

1.2 Simulationg Electrical Activation

1.2.1 Governing Equations

Electrical activation throughout the ventricular model was simulated using the bidomain equations [4]

$$\begin{aligned}
\nabla \cdot \boldsymbol{\sigma_i} \nabla \phi_i &= \beta I_m && (1)\\
\nabla \cdot \boldsymbol{\sigma_e} \nabla \phi_e &= -\beta I_m - I_{ei} && (2)\\
I_m &= C_m \frac{\partial V_m}{\partial t} + I_{ion}(V_m, \boldsymbol{\eta}) - I_s && (3)\\
\nabla \cdot \sigma_b \nabla \phi_e &= -I_{eb} && (4)
\end{aligned}$$

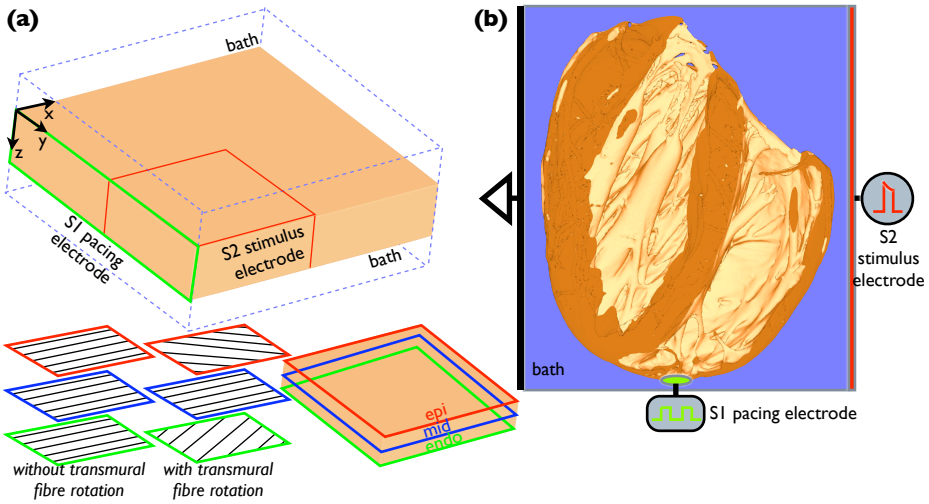

Figure 1: (a) Simplified slab model showing location of surrounding conducting bath in z-direction (blue wire-frame), S1 (green) and S2 (red) stimulation sites, as well as schematic representation of fibre architecture for the two scenarios with and without transmural fibre rotation. (b) Whole-ventricular model shown from a posterior view with a clipping plane to expose endocardial structures, showing locations of S1 (green) and S2 (red) stimulation sites.

where ϕ_i and ϕ_e are the intracellular and extracellular potentials, respectively, $V_m = \phi_i - \phi_e$ is the transmembrane voltage, $\boldsymbol{\sigma_i}$ and $\boldsymbol{\sigma_e}$ are the intracellular and extracellular conductivity tensors, respectively, β is the bidomain membrane surface to volume ratio, I_m is the transmembrane current density, I_{ei} and I_{eb} are extracellular stimuli applied in the interstitial space or the bath, respectively, I_s is a transmembrane stimulus, C_m is the membrane capacitance per unit area, and I_{ion} is the membrane ionic current density which depends on V_m and a set of state variables $\boldsymbol{\eta}$. At tissue boundaries, no flux boundary conditions are approximated for ϕ_i

$$\boldsymbol{\sigma_i} \nabla \phi_i \cdot \mathbf{n} = 0, \tag{5}$$

as well as continuity of ϕ_e and the normal component of the extracellular current

$$\phi_e = \phi_{eb} \tag{6}$$

$$\boldsymbol{\sigma_e} \nabla \phi_e \cdot \mathbf{n} = \sigma_b \nabla \phi_e \cdot \mathbf{n}. \tag{7}$$

At the boundaries of the conductive bath surrounding the tissue, no flux boundary conditions for ϕ_e are imposed

$$\sigma_b \nabla \phi_e \cdot \mathbf{n} = 0. \tag{8}$$

1.2.2 Electrical Model Parameters

Cell membrane dynamics were represented by a recent rabbit ventricular cell model [5]. Intra- and extracellular conductivities were based-on those of Roberts & Scher (1982) [6] being 0.34 and 0.12 S/m along the myofibre direction and 0.060 and 0.080 S/m normal to the fibre direction, respectively, which were then uniformly scaled to reduce conduction velocity by 25% to replicate the slowed conduction seen during arrhythmias and rapid pacing [7, 8]. Such a reduction is made to account for the experimentally-observed lateralization and hypophosphorylation of Cx43 during heart failure which controls the flow of current between cells [9, 10]. We chose to reduce CV in our model to replicate this slowing of conduction during pathological conditions due to

our direct focus upon arrhythmia mechanisms throughout the study. Similar reductions in CV have been widely made previously for similar reasons [11, 12]. Conductivity of the extracellular bath (g_b) was 1.0 S/m (isotropic). Tissue was classified as excitable if $V_m < -60$mV, the threshold for inactivation of the sodium current [13].

1.2.3 Induction of Arrhythmias

Episodes of arrhythmias were induced using a standard S1-S2 protocol, as follows. In the slab, an S1 pacing stimulus (applied to the $x = 0$ face) was followed a given coupling interval (CI) later by a transmembrane S2 stimulus applied to the lower quadrant of tissue. In the whole ventricular model, the S1 pacing stimulus was applied at the apex with the S2 stimulus applied a CI later as an external extracellular shock of shock strength (SS) 10 V ($\sim$ 4 V/cm) via two plate-electrodes in the anterior-posterior configuration. Electrode set-ups and stimulus sites are shown in Figure 1.

1.2.4 Computational Considerations

The bidomain equations were solved with the Cardiac Arrhythmia Research Package (CARP) [14]. The specifics of the numerical regimes used in CARP have been described extensively elsewhere [15, 16]. Simulations were performed on both European SP6 DEISA HPC and Oxford Supercomputing Centre facilities. Visualisation of results was performed with the Meshalyzer software.

1.2.5 Mesh Discretization

Simulations within the slab model were performed at a mesh discretisation level of 200 μm. Tests have shown that deviations in CV from the fully converged solutions (approximately $h < 100$ μm) were minor in both the longitudinal and transverse directions using the non-mass lumping finite element configuration set-up. However, these uncertainties are very minor in the context of the overall uncertainties in the parameters of the bidomain model, and importantly would be consistent throughout all simulations performed on the slab models. Mesh discretisation was restricted to 200 μm as finer levels would have produced meshes with significantly more degrees of free requiring infeasible computational loads in the simulation of long-duration sustained reentrant activity performed in this study.

1.3 Filament Detection and Analysis

1.3.1 Filament Detection Algorithm

The algorhim used for filament detection was based-on the approach of Fenton & Karma (1998) [1], adapted for use within an unstructured finite element regime. The method defines the location of a filament as the intersection of the isosurfaces of $V_m = V_{iso}$ and $\frac{dV_m}{dt} = 0$. If an intersection is found to occur within a finite element, the coordinates of the point of entry and exit of the filament section through the element are computed. Optimised values of $dt = 8$ ms (the time-delay over which $\frac{dV_m}{dt} = 0$ is computed) and $V_{iso} = -40$ mV were found specifically for the cell model used [5].

1.3.2 Analysis of Filament Dynamics

The methods for identifying individual filaments in space and tracking their dynamics in time were based upon previous studies [17, 18] (which used regular voxel-based grids), adapted for

use on unstructured finite element meshes used in this study. Briefly, individual filaments were defined by joining all neighbouring elements (directly connected through shared nodes) containing a filament section and assigned a unique identifying tag. The length of individual discrete filaments was calculated by summing the total number of elements defining it, as in [2].

Temporal filament dynamics were analysed by examining individual filament over-lap in successive time-steps. Filaments interaction events were defined by: (i) *birth*, filament present at time $t+1$ does not over-lap with any filaments in time t; (ii) *death*, filament present at t does not over-lap with any filaments in $t+1$; (iii) *amalgamation*, filament at $t+1$ over-laps with >1 filament at t; (iv) *division*, filament at t over-laps with >1 filament at $t+1$; (v) *continuation*, filament at t over-laps with single filament at $t+1$. As in [17], accurate filament over-lap between time-steps was ensured by first smoothing filaments in space, involving expanding-out individual filaments in all directions to also include neighbouring elements with direct node connectivity.

Following the procedure of [18], if a filament continues, the unique identifying tag is simply inherited by the over-lapping filament. If a filament is born, it gets a new tag; if it dies, the tag is not re-used. If a filament divides, the longest of the new filaments at $t+1$ inherits the original tag, whilst the remaining shorter filaments are given new tags. If filaments amalgamate, the new filament at $t+1$ inherits the tag of the longest of the old filaments. Throughout each simulation, all filament interactions (birth, death, division and amalgamation) were recorded along with total filament numbers and mean lengths at each time-step. Total filament interaction rate was defined as the sum of the birth, death, division and amalgamation rates.

2 Results

2.1 Dependence of Bath-Loading Effects During Pacing Upons Specific Conductivity Set Values

In the manuscript, we focus soley on analysing the implications of bath-loading when using one specific set of conductivity parameters - those obtained by Roberts & Scher (1982) [6]. This set was chosen as we had previously demonstrated that these particular values produced the most significant bath-loading induced changes in wavefront morphology in highly simplified pseudo-2D models [19]. In our previous study [19], we defined a metric R which defined the ratio of the conductivity of the tissue close to the edge (in contact with the perfusing bath) to that within the tissue bulk. and thus was a function of the intra- and extracellular conductivities defined by a particular set. R was seen to be closely related to the magnitude of the tissue-bath effect witnessed upon the activation wavefront during propagation. The value of R found for the Roberts & Scher (1982) [6] set was 1.65/2.76 in the cross-fibre/fibre directions, respectively. The subsequent analysis conducted in this study thus sought to provide an upper-limit on the possible implications of bath-loading effects during arrhythmias by using the Roberts & Scher (1982) values.

However, it is an interesting question of how the use other standard conductivity sets within the bidomain model impact wavefront morphology via the bath-loading mechanism within the context of increased anatomical heterogeneity, such as transmural fibre rotation, not considered previously [19]. Therefore, the pacing simulations using the slab model (both with and without transmural fibre rotation) were repeated using the Clerc (1976) [20] and Roberts *et al* (1979) [21] conductivity sets, which have respective R values of 1.06/1.12 and 1.15/1.78 in the cross-fibre/fibre directions. The results from these simulations are shown below in Figure 2 (Clerc (1976)) and Figure 3 (Roberts *et al* (1979)), showing the V_m distributions within the slab models without (panel a) and with (panel b) transmural fibre rotation 50 ms following pacing stimulus.

As before, top panel shows stimulus along $x = 0$ cm plane, inducing wavefront propagation *along* the fibre direction; bottom panel shows stimulus along $y = 3$ cm plane, inducing propagation *perpendicular* to fibres. Note that, as with the conductivity values of Roberts & Scher (1982) [6] used in the manuscript , here conductivity values have been slightly scaled so as to reduced CV by 25%, as witnessed during heart failure (discussed in Section 1.2.2).

Figure 2(a) shows that, in the case of no transmural fibre rotation, the Clerc (1976) conductivity set produces only a very slight bath-loading effect on wavefront morphology, similar to that witnessed previously [19]. In the case of transmural fibre rotation (panel b), in absence of the bath (BDMNB, left) the wavefront is seen to have a highly curved nature for both propagation directions (convex for along-fibre stimulus, concaved for cross-fibre stimulus). [This curvature in the BDMNB case is more significant than that seen in the manuscript when using the Roberts & Scher (1982) [6] conductivities due to the higher anisotropy ratio (8.9 intracellular, 2.6 extracellular) of Clerc (1976) compared to Roberts & Scher (1982) (5.7, 1.5, respectively).] Due to the small bath-loading effect seen in panel (a), the inclusion of the bath in panel (b) is not seen to have a significant effect on wavefront morphology: the convex wavefront is very slightly attenuated, with the concave wavefront slightly accentuated. Thus, there are very little differences between the presence and absence of the bath.

In the case of Figure 3, a more significant bath-loading effect is seen both in the presence and absence of transmural fibre rotation. In panel (b), as anisotropy ratios are similar to the Clerc (1976) set (10.8 intracellular, 1.7 extracellular), a pronounced curvature is seen in the absence of the bath purely due to fibre rotation. However, the increased bath-loading effects seen in panel (a) then lead to a noticeable attenuation of the convex wavefront and accentuation of the concaved wavefront, although, as expected, neither of which are as significant as shown in the manuscript with the Roberts & Scher (1982) conductivities.

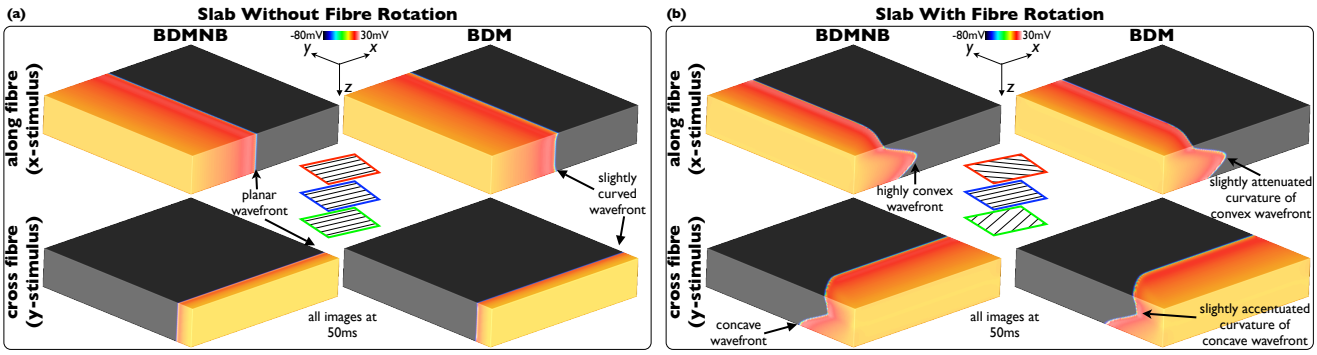

Figure 2: Effects of bath-loading during pacing in the slab model without (panel a) and with (panel b) transmural fibre rotation with conductivity values based-on those of Clerc (1976) [20]. In each panel V_m distributions for BDMNB (left) and BDM (right), 50 ms following pacing stimulus along x = 0 (top) and y = 3 cm (bottom) planes.

2.2 Dependence of Bath-Loading Effects During Pacing Upon Specific Conduction Velocity

As described above, conductivities were adjusted throughout to reproduce the reduction in CV of approximately 25% commonly witnessed during pathological conditions [9, 10]. Here, we access how this reduction in CV from the standard Roberts & Scher (1982) conductivity set may influence the resulting bath-loading effects on wavefront morphology, the implications of which are analysed throughout this study. The pacing simulations using the slab model (both

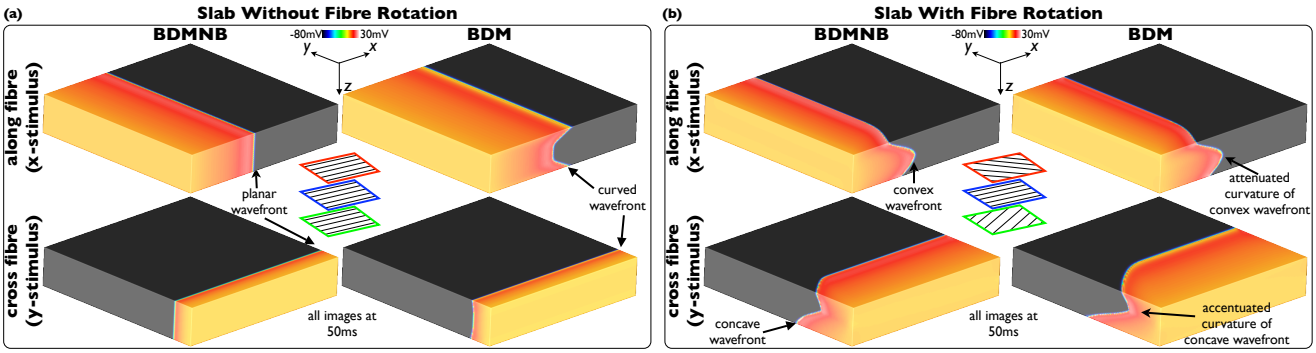

Figure 3: Effects of bath-loading during pacing in the slab model without (panel a) and with (panel b) transmural fibre rotation with conductivity values based-on those of Roberts *et al.* (1979) [21]. In each panel V_m distributions for BDMNB (left) and BDM (right), 50 ms following pacing stimulus along x = 0 (top) and y = 3 cm (bottom) planes.

with and without transmural fibre rotation) were again repeated this time using the standard Roberts & Scher (1982) conductivity set [6] with no alterations to reduce CV. Figure 4 shows the V_m distributions within the slab models without (panel a) and with (panel b) transmural fibre rotation 50 ms following pacing stimulus applied along $x = 0$ cm plane (top) and along with $y = 3$ cm plane (bottom). In addition to the expected increase in CV, the panels of Figure 4 demonstrate very similar bath-loading effects upon wavefront morphology to those witnessed in the manuscript for the case of the reduced CV parameter set (Figures 2 & 4 in the manuscript).

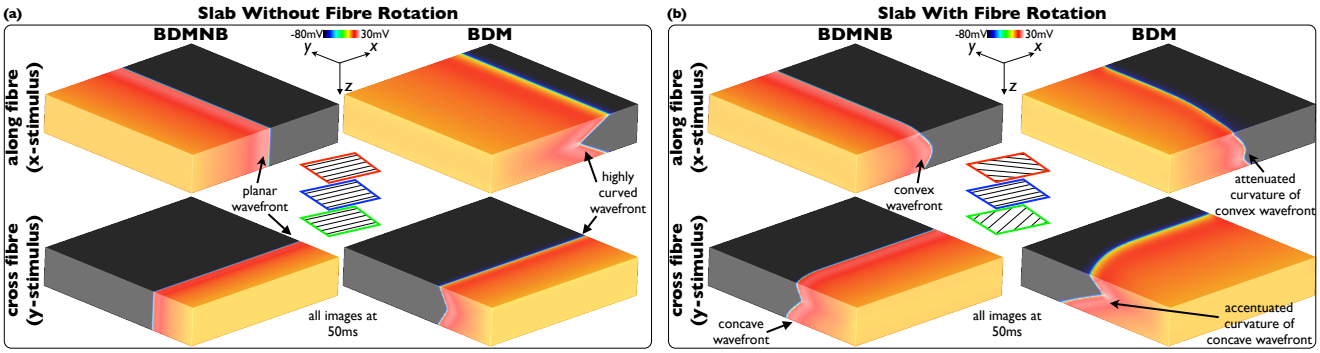

Figure 4: Effects of bath-loading during pacing in the slab model without (panel a) and with (panel b) transmural fibre rotation with conductivity values given exactly by Roberts & Scher (1982) [6] In each panel V_m distributions for BDMNB (left) and BDM (right), 50 ms following pacing stimulus along x = 0 (top) and y = 3 cm (bottom) planes.

2.3 Mechanism of Survival of Arrhythmias within Whole Ventricular Model in the Presence of a Bath

The majority of cases of arrhythmias induced in the whole-ventricular BDM model terminated soon after induction, as described in Section 3.3.2 of the manuscript, with only 5 instances being sustained for more than one reentrant cycle. In such instances which were sustained, although wavefront propagation around the LV free wall was blocked (in a similar manner to those cases in which reentry terminated) a small excitable gap was seen to exist within the

endocardial structures on the thick LV wall which allowed propagation to continue, causing reentry to be sustained. The existance of such an excitable path is shown in Figure 5 for the episode CI = 180 ms, demonstrating how propagation is sustained.

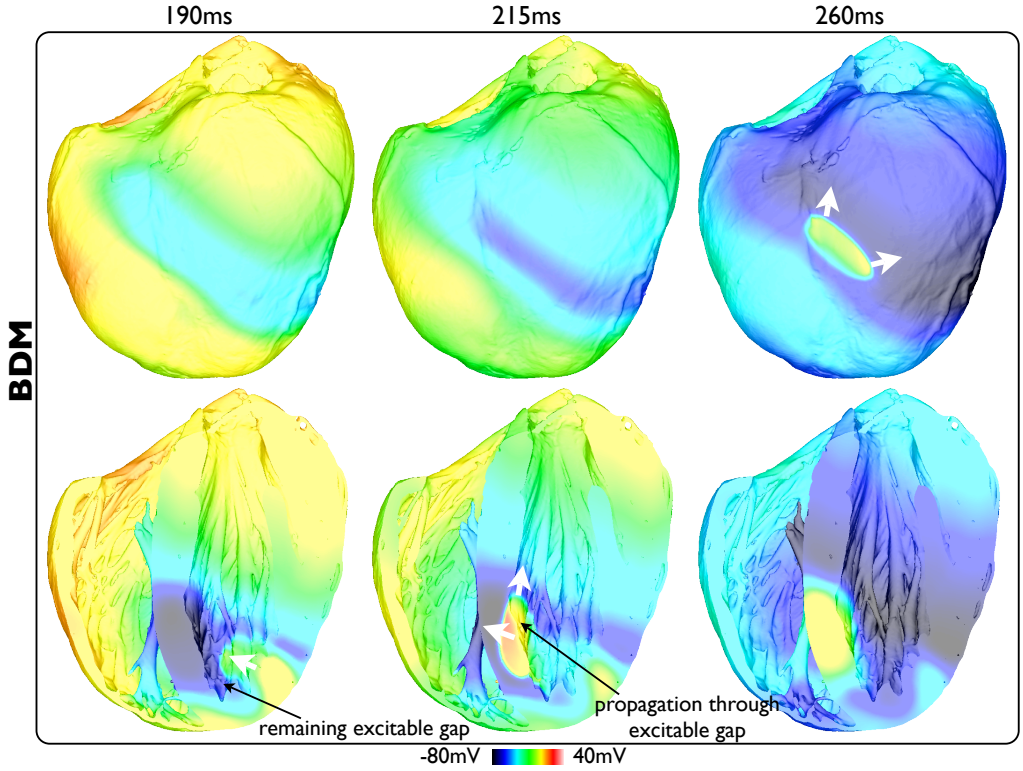

Figure 5: V_m distributions within the volume of the ventricles at certain time instances following arrhythmia induction with CI = 180 ms in the BDM case shown in anterior epicardial views (top row), as wel as views taken with an axial slice to expose posterior endocardial surfaces and septum (bottom row), are shown. White arrows show direction of wavefront propagation.

2.4 Filament Dynamics in Sustained Episodes of Arrhythmias within the Whole Ventricles

For those instances of arrhythmias which were induced within the whole ventricular model, filament dynamics were analysed throughout the duration of each episode. This constituted 3 sustained episodes in the BDM case, and 9 in the BDMNB case. The table given below in Figure 6 gives detailed filament statistics concerning mean/max filament numbers, mean lengths, total interaction rates, total numbers of filaments produced as well as the duration of each arrhythmia episode.

References

[1] Fenton, F., and A. Karma. 1998. Vortex dynamics in three-dimensional continuous myocardium with fiber rotation: filament instability and fibrillation. *Chaos*. 8:20–47.

[2] Clayton, R. 2008. Vortex filament dynamics in computational models of ventricular fibrillation in the heart. *Chaos*. 18:043127.

		total int. rate	mean no. ± sd	max no.	total filaments	total filaments /ms	mean length ± sd	duration
BDM	**CI 180**	0.851	3.66 ± 1.81	11	311	0.43	178 ± 117	923ms
	CI 220	1.085	4.94 ± 2.47	15	991	0.55	154 ± 95	2008ms
	CI 235	0.866	3.61 ± 2.03	13	445	0.44	164 ± 92	1173ms
BDMNB	**CI 180**	1.186	5.57 ± 2.73	17	769	0.60	106 ± 59	1488ms
	CI 185	1.403	6.19 ± 2.56	15	528	0.70	118 ± 61	939ms
	CI 190	0.948	4.13 ± 2.73	15	398	0.48	88 ± 65	1041ms
	CI 195	1.144	5.33 ± 4.16	20	788	0.57	81 ± 47	1568ms
	CI 200	0.870	3.99 ± 3.25	17	693	0.43	62 ± 50	1832ms
	CI 205	1.183	4.85 ± 3.00	18	553	0.60	114 ± 61	1128ms
	CI 210	1.141	4.69 ± 2.54	13	578	0.58	114 ± 62	1200ms
	CI 230	1.014	4.02 ± 2.36	17	474	0.52	115 ± 70	1151ms
	CI 240	1.131	5.50 ± 2.75	16	789	0.57	102 ± 52	1599ms

Figure 6: Filament statistics for episodes of sustained arrhythmias within the whole-ventricular model for BDM (3 episodes) and BDMNB (9 episodes) cases.

[3] Bishop, M., G. Plank, R. Burton, J. Schneider, D. Gavaghan, V. Grau, and P. Kohl. 2010. Development of an anatomically-detailed mri-derived rabbit ventricular model and assessment of its impact on simulation of electrophysiological function. *Am J Physiol Heart Circ Physiol.* 298:H699–H718.

[4] Henriquez, C. 1993. Simulating the electrical behavior of cardiac tissue using the bidomain model. *Crit Rev Biomed Eng.* 21:1–77.

[5] Mahajan, A., Y. Shiferaw, D. Sato, and A. Baher. 2008. A rabbit ventricular action potential model replicating cardiac dynamics at rapid heart rates. *Biophys J.* 94:392–410.

[6] Roberts, D., and A. Scher. 1982. Effect of tissue anisotropy on extracellular potential fields in canine myocardium in situ. *Circ Res.* 50:342–51.

[7] Banville, I., and R. Gray. 2002. Effect of action potential duration and conduction velocity restitution and their spatial dispersion on alternans and the stability of arrhythmias. *J Cardiovasc Electrophysiol.* 13:1141–1149.

[8] Cao, J. M., Z. Qu, Y. H. Kim, T. J. Wu, A. Garfinkel, J. N. Weiss, H. S. Karagueuzian, and P. S. Chen. 1999. Spatiotemporal heterogeneity in the induction of ventricular fibrillation by rapid pacing: importance of cardiac restitution properties. *Circulation Research.* 84:1318–31.

[9] Akar, F., D. Spragg, R. Tunin, D. Kass, and G. Tomaselli. 2004. Mechanisms underlying conduction slowing and arrhythmogenesis in nonischemic dilated cardiomyopathy. *Circ Res.* 95:717.

[10] Akar, F., R. Nass, S. Hahn, E. Cingolani, M. Shah, G. Hesketh, D. Disilvestre, R. Tunin, D. Kass, and G. Tomaselli. 2007. Dynamic changes in conduction velocity and gap junction properties during development of pacing-induced heart failure. *Am J Physiol Heart Circ Physiol.* 293:H1223.

[11] Constantino, J., V. Gurev, and N. Trayanova. 2011. Cardiovascular Multimodal Image-Guided Diagnosis and Therapy, chapter 13: Electromechanical Modeling Applied to Cardiac Resynchronization Therapy. McGraw Hill.

[12] A Sambelashvili, I. E. 2004. Dynamics of virtual electrode-induced scroll-wave reentry in a 3d bidomain model. *AJP: Heart Circ Physiol.* 287:H1570–H1581.

[13] Constantino, J., Y. Long, T. Ashihara, and N. Trayanova. 2010. Tunnel propagation following defibrillation with icd shocks: Hidden postshock activations in the left ventricular wall underlie isoelectric window. *Heart rhythm.* 7:953–961.

[14] Vigmond, E., M. Hughes, G. Plank, and L. Leon. 2003. Computational tools for modeling electrical activity in cardiac tissue. *J Electrocardiol.* 36:69–74.

[15] Plank, G., M. Liebmann, R. Weber dos Santos, E. J. Vigmond, and G. Haase. 2007. Algebraic multigrid preconditioner for the cardiac bidomain model. *IEEE Trans Biomed Eng.* 54:585–596.

[16] Vigmond, E. J., R. Weber dos Santos, A. J. Prassl, M. Deo, and G. Plank. 2008. Solvers for the cardiac bidomain equations. *Prog Biophys Mol Biol.* 96:3–18.

[17] Clayton, R., and A. Holden. 2002. A method to quantify the dynamics and complexity of re-entry in computational models of ventricular fibrillation. *Phy Med & Biol.* 47:225–238.

[18] Tusscher, K. T., R. Hren, and A. Panfilov. 2007. Organization of ventricular fibrillation in the human heart. *Circ Res.* 100:e87–e101.

[19] Bishop, M., and G. Plank. 2010. Representing the cardiac bath-loading effect with an augmented monodomain equivalent model. *IEEE Trans Biomed Imag.* 58:1066–75.

[20] Clerc, L. 1976. Directional differences of impulse spread in trabecular muscle from mammalian heart. *J Physiol (Lond).* 255:335–46.

[21] Roberts, D. E., L. T. Hersh, and A. M. Scher. 1979. Influence of cardiac fiber orientation on wavefront voltage, conduction velocity, and tissue resistivity in the dog. *Circ Res.* 44:701–12.